Supporting Information

Bassett et al. 10.1073/pnas.0911346107

SI Materials and Methods

D2KO and D1/D2KO Mice. WT mice, mice deficient in type 2 deiodinase (D2KO), and mice deficient in type 1 deiodinase (D1KO) mice were established in a C57BL/6J background and maintained as homozygous colonies (1, 2). D2KO and D1KO mice were crossed to obtain double-heterozygous F1 progeny, which were bred to maintain a colony of D1/D2KO homozygous double mutants. Mice were housed under conditions of controlled lighting and temperature. Some mice were given two i.p. injections of calcein (15mg/kg in saline with 2% NaHCO3) 7 and 4 days before killing at postnatal day (PD) 112. Adult male WT mice were rendered hypothyroid or thyrotoxic for 6 weeks. Hypothyroidism was induced by feeding a low-iodine diet supplemented with 0.15% propylthiouracil (Harlan Teklad Co). Thyrotoxicosis was induced by suppressive doses of thyroxine (T4) (0.0012%) in the drinking water. The concentration of T4 was adjusted according to intake in 2-week cycles (3). Serum free T4 and free 3, 5, 3′-L-triiodothyronine (T3) levels were measured on an Abbott ARCHITECT i2000 auto-analyzer (Abbott Laboratories); interassay coefficients of variation (CV) were below 10.4%, 10.0%, and 4.0%, respectively.

Faxitron Point Projection Microradiographic Analysis. Long bones and tail vertebrae were stored in 70% ethanol at 4 °C. Soft tissue was removed, and digital x-ray images were recorded at 10-μm pixel resolution using a Qados Faxitron MX20 variable kV point projection x-ray source and digital image system operating at 26 kV and 5× magnification (Cross Technologies plc). Magnifications were calibrated by imaging a digital micrometer, and long bone lengths were determined using ImageJ 1.41 software (http://rsb.info.nih.gov/ij/). Cortical bone thickness and diameter were determined in at least 10 locations at the midfemoral diaphysis in both anterior–posterior and medial–lateral projections. The relative mineral content of calcified tissues was determined by comparison with the following standards included in each image frame: a 1-mm thick steel plate, a 1-mm diameter spectrographically pure aluminum wire, and a 1-mm diameter polyester fiber. Sixteen-bit (2368 × 2340) DICOM images were converted to 8-bit Tiff images using ImageJ, and the histogram stretched from the polyester (gray level 0) to the steel (gray level 255) standards. Increasing gradations of mineralization density were represented in 16 equal intervals by a pseudocolor scheme for presentation of digital images.

Quantitative Backscattered Electron Scanning Electron Microscopy Analysis of Bone Mineralization. The distribution of bone micromineralization densities was analyzed at cubic-micrometer voxel resolution by quantitative backscattered electron scanning electron microscopy (qBSE-SEM) (4–6). Bones were fixed in 10% neutral buffered formalin for 24 h and transferred to 70% ethanol before embedding in polymethyl methacrylate (PMMA). Block faces were cut through specimens, which then were polished, coated with carbon, and analyzed in a Zeiss DSM962 digital scanning electron microscope equipped with an annular solid-state BSE detector (KE Electronics) and operated at 20 kV and 0.5 nA at a 17-mm working distance (11 mm sample to detector). Mineralization densities were determined by comparison with halogenated dimethacrylate standards: $C_{22}H_{25}O_{10}Br$ [mean BSE coefficient according to the procedure of Lloyd (7) = 0.1159] to $C_{22}H_{25}O_{10}I$ (mean BSE coefficient = 0.1519). Increasing gradations of micromineralization density were represented in eight equal intervals by a pseudocolor scheme (4–6).

MicroCT Analysis. Tibias from WT and D1/D2KO mice were analyzed by microCT (Skyscan 1172a) at 50 kV and 200 μA using a 0.5-mm aluminum filter and a detection pixel size of $4.3 \ \mu m^2$. Images were captured every 0.7° through 180° rotation of each bone. Scanned images were reconstructed using Skyscan NRecon software. A volume of 1 mm^3 of trabecular bone was selected as the region of interest, 0.2 mm from the growth plate. Trabecular bone volume as proportion of tissue volume (BV/TV, %), trabecular thickness (Tb.Th, mm), trabecular separation (Tb.Sp, mm), trabecular number (Tb.N, mm^{-1}), and structure model index (SMI) were analyzed in the region of interest using the Skyscan CT analysis software.

Mechanical Testing. Femurs from PD112 mice were stored and tested in 70% ethanol. The anterior–posterior middiaphyseal cortical thickness (Tap) and diameter (Dap), and the medial–lateral cortical thickness (Tml) and diameter (Dml) of individual bones were determined in Faxitron images using ImageJ. Destructive three-point bend tests were performed on an Instron 5543 materials-testing load frame (Instron Limited) using custom-built mounts incorporating rounded supports to minimize cutting and shear loads. Biomechanical variables can be derived from load displacement curves and cortical bone thickness measurements (8–11). Bones were positioned horizontally and centered on custom supports with the anterior surface upward. Load (F) was applied vertically to the midshaft with a constant rate of displacement of 0.03 mm/second until fracture. A span (L) of 5.6 mm was used. Load-displacement curves were plotted, and yield load (Fy), displacement at yield (δ), maximum load (Fm), and fracture load (F#) were determined. Stiffness, i.e., the slope of the linear (elastic) part of the load–displacement curve, was calculated by the least squares method. The moment of inertia (I: second moment of area) was calculated by adding the cylindrical and upper and lower linear components: I-total = I_{tube} + I_{linear}. The cylindrical component was calculated according to the formula $I_{tube} = Tml \times r^3 \times \pi$ where r = (Dap/2) − (Tml/2). The linear component was calculated according to the formula $I_{linear} = 2(Dml − Dap) \times Tap$ [(Dap − Tap)²/4] (Fig. S1A). Young's modulus (E) was calculated according to the formula $E = Fy \times L^3/\delta \times 48 \times I_{total}$. Yield stress (σy) was calculated according to the formula $\sigma y = Fy \times L \times (Dap/2)/4 \times I_{total}$. Work energy was calculated from the area under the load displacement curve at both maximum load and fracture. Elastic stored energy at maximum load was determined by calculating the area of a right-angled triangle with the vertex at the point of maximum load and a hypotenuse with a slope equal to that of the linear phase of the load–displacement curve (Fig. S1B). Elastic stored energy at fracture was calculated similarly but with the vertex of the triangle at the point of fracture. Energy dissipated at maximum load was calculated by subtracting the elastic stored energy from the work energy at maximum load. Crack toughness was determined by dividing the energy dissipated at fracture by the area of the fracture surface.

Skeletal Preparations. PD1 mice and limbs from PD14, PD21, PD28, PD56, and PD112 animals were stained with alizarin red and Alcian blue and cleared in KOH glycerol (12, 13). Preparations were photographed using a Leica MZ75 binocular microscope (Leica AG), Leica KL1500 light source, Leica DFC320 digital camera, and Leica IM50 Digital Image Manager. Bone lengths were determined digitally following linear calibration of pixel size. Skull dimensions and open fontanel and suture areas were calculated using Image J.

Histology. Limbs were fixed in 10% neutral buffered formalin for 24 h and decalcified in 10% formic acid or 10% EDTA. PD1 limbs were decalcified for 24 h; PD14, PD21, and PD28 limbs were decalcified for 5 days; and PD56 and PD112 limbs were decalcified for 7–10 days. Decalcified bones were embedded in paraffin, and 3-μm sections were cut onto 3-aminopropyltriethoxysilane (APES)–coated slides (Sigma-Aldrich Chemical Company), deparaffinized in xylene, rehydrated, and stained with van Gieson and Alcian blue.

Histological Analysis of Growth Plate and Cortical Bone Dimensions. Collagen II and collagen X mRNA expression was analyzed by in situ hybridization to identify proliferative and hypertrophic zones in growth plate sections, as described in previous studies in which methods were optimized (14–17), and expression of the T3 target gene *Fgfr1* was determined to characterize cellular thyroid status in osteoblasts and chondrocytes (18, 19). Measurements of at least four separate positions across the width of growth plates were obtained using a Leica DM LB2 microscope and Leica DFC320 digital camera to calculate mean values for the heights of the reserve zone, proliferative zone, hypertrophic zone, and total growth plate in sections of proximal tibia. Results from two different levels of sectioning were compared to ensure consistency of the data. Cortical bone measurements were performed in longitudinal and transverse sections. At least 10 separate positions in the midshaft of long bones were analyzed, and adjacent levels of sectioning were compared to ensure consistency.

Measurement of Bone Turnover Markers. Serum samples were obtained from P91 WT and D1/D2KO mice at sacrifice and were stored at −80 °C. N-terminal propeptide of type 1 procollagen (P1NP) and C-terminal cross-linked telopeptide of type I collagen (CTX) levels were determined by enzyme immunoassay using IDS kits AC-33F1 and AC-06F1, respectively (Immunodiagnostic Systems). Osteocalcin levels were determined by immunoradiometric assay using the Immutopics kit 50–1300 (Immutopics). Tartrate-resistant acid phosphatase form 5b (TRAP) levels were determined by a solid-phase immunofixed enzyme activity assay using the IDS kit SB-TR103. All assays were performed according to manufacturers' instructions.

Osteoclast Histomorphometry. Osteoclast numbers were determined in samples fixed for 48 h in 10% neutral buffered formalin and decalcified in 10% EDTA, pH 7.4, for 28 days. Decalcified bones were embedded in paraffin, and 3-μm midline longitudinal sections were cut onto Superfrost plus slides (VWR Limited). Sections were deparaffinized, rehydrated, and stained for TRAP using a Sigma TRAP kit (386A-1KT) according to manufacturer's instructions, except that fast garnet dye was diluted 10-fold, and the incubation time was 20 min. Sections were photographed at ×200 magnification using a Leica DM LB2 microscope and DFC320 digital camera, and a montage of nine overlapping fields was constructed for each bone. Osteoclast numbers (Oc.N) and surface (Oc.S) were determined in both trabecular and endosteal bone and were normalized to total bone surface. All measurements were commenced 500 μm inferior to the growth plate (14, 15).

BSE-SEM Analysis of Bone Surfaces and Microarchitecture. Freshly dissected bones were fixed and stored in 70% ethanol. Bones were opened longitudinally along anatomical curvatures using a fine tungsten carbide milling tool in a dental workshop handpiece to remove half the cortical bone and medullary trabecular elements. Samples were cleaned of cell remnants by maceration with an alkaline bacterial pronase, which also removes unmineralized cartilage matrix. Samples were coated with carbon and imaged using backscattered electrons at 20-kV beam potential. The images provide detailed views of bone surfaces and microarchitecture from which surface activity states (forming, resting, resorbing, resorbed) can be investigated (20, 21).

Confocal Microscopy Analysis of Bone Formation. Midline longitudinal and midcoronal block faces were cut through PMMA-embedded long bones and calvaria. Specimens were polished to an optically flat finish and examined using confocal autofluorescence scanning light microscopy (CSLM) of calcein labels to determine the fraction of bone surface undergoing active bone formation (22). Two systems were used: (*i*) an Odyssey (Noran) microscope using 488-nm excitation, a 60×/1.4NA objective, and a pass filter, and (*ii*) a Leica SP2 reflection confocal microscope using 488-nm excitation and 25×/1.0 and 40×/1.25 objectives, which generated combined reflection (blue), calcein fluorescence (green), and autofluorescence (red) CSLM images. Tissue layers immediately deep to the block surface were visualized to ensure that only fluorescently labeled bone-forming surfaces that lie in orthogonal planes were analyzed (6, 23, 24). Calcein separation in trabecular and calvarial bone was measured from the Odyssey images using a TN8500 image processor (Noran). The mineral apposition rate (MAR) was calculated by determining calcein separation at 10 to 20 locations per specimen. Montages of trabecular and calvarial bone were generated, and the bone surface and mineralizing surface were measured using ImageJ. Montages of 12 (magnification ×25) or 20 (magnification ×40) overlapping CSLM fields also were constructed for each bone. Trabecular and endosteal bone surfaces were determined using ImageJ. Mineralizing surface and MAR were determined by quantifying calcein-labeled surfaces and the mean separation between calcein double labels. Bone formation rate was calculated from the product of mineralizing surfaces and MAR. All measurements commenced 500 μm inferior to the growth plate.

Osteoblast Histomorphometry. Midline sagittal sections (5 μm) were cut from PMMA-embedded specimens using a Leica RM2245 microtome. Sections were mounted on Fol's coated slides [1.5% gelatin, 1% CrK(SO$_4$)$_2$ in 30% ethanol], incubated at 37 °C overnight, deplasticized in Cellosolve (Sigma), rehydrated in graded ethanols, and stained with toluidine blue (2% toluidine blue in 5 mM disodium hydrogen phosphate, 8 mM citric acid, pH 3.7) for 5 min before destaining in butanol and toluidine blue buffer. Sections were imaged with a Leica DM LB2 microscope and DFC320 digital camera using a 20×/0.40 objective. Montages of metaphyseal trabecular bone were generated, and at least two different levels of section were compared to ensure consistency of data. Primary histomorphometric indices of bone formation were determined using ImageJ according to the standard American Society for Bone and Mineral Research system of nomenclature (25).

Statistical Analysis. Normally distributed data were analyzed by Student's *t* test or ANOVA followed by Tukey's multiple comparison post hoc test. *P* values <0.05 were considered significant. Frequency distributions of bone micromineralization densities obtained by Faxitron and qBSE were compared using the Kolmogorov-Smirnov test, in which *P* values for the *D* statistic in 1024-pixel data sets were $D \geq 6.01$, $P < 0.05$; $D \geq 7.20$, $P < 0.01$; and $D \geq 8.62$, $P < 0.001$.

1. Schneider MJ, et al. (2001) Targeted disruption of the type 2 selenodeiodinase gene (DIO2) results in a phenotype of pituitary resistance to T4. *Mol Endocrinol* 15: 2137–2148.
2. Schneider MJ, et al. (2006) Targeted disruption of the type 1 selenodeiodinase gene (Dio1) results in marked changes in thyroid hormone economy in mice. *Endocrinology* 147:580–589.
3. Weiss RE, et al. (1998) Thyroid hormone action on liver, heart, and energy expenditure in thyroid hormone receptor beta-deficient mice. *Endocrinology* 139:4945–4952.
4. Boyde A, Firth EC (2005) Musculoskeletal responses of 2-year-old Thoroughbred horses to early training. 8. Quantitative back-scattered electron scanning electron microscopy and confocal fluorescence microscopy of the epiphysis of the third metacarpal bone. *N Z Vet J* 53:123–132.

5. Boyde A, Jones SJ, Aerssens J, Dequeker J (1995) Mineral density quantitation of the human cortical iliac crest by backscattered electron image analysis: Variations with age, sex, and degree of osteoarthritis. *Bone* 16:619–627.

6. Boyde A, Travers R, Glorieux FH, Jones SJ (1999) The mineralization density of iliac crest bone from children with osteogenesis imperfecta. *Calcif Tissue Int* 64:185–190.

7. Lloyd GE (1987) Atomic number and crystallographic contrast images with the SEM: A review of backscattered electron techniques. *Mineral Mag* 51:3–19.

8. Schriefer JL, et al. (2005) A comparison of mechanical properties derived from multiple skeletal sites in mice. *J Biomech* 38:467–475.

9. Silva MJ, Brodt MD, Uthgenannt BA (2004) Morphological and mechanical properties of caudal vertebrae in the SAMP6 mouse model of senile osteoporosis. *Bone* 35:425–431.

10. Dai XM, Zong XH, Akhter MP, Stanley ER (2004) Osteoclast deficiency results in disorganized matrix, reduced mineralization, and abnormal osteoblast behavior in developing bone. *J Bone Miner Res* 19:1441–1451.

11. Flenniken AM, et al. (2005) A Gja1 missense mutation in a mouse model of oculo-dentodigital dysplasia. *Development* 132:4375–4386.

12. O'Shea PJ, et al. (2005) Contrasting skeletal phenotypes in mice with an identical mutation targeted to thyroid hormone receptor alpha1 or beta. *Mol Endocrinol* 19:3045–3059.

13. O'Shea PJ, et al. (2003) A thyrotoxic skeletal phenotype of advanced bone formation in mice with resistance to thyroid hormone. *Mol Endocrinol* 17:1410–1424.

14. Bassett JH, et al. (2007) Thyroid status during skeletal development determines adult bone structure and mineralization. *Mol Endocrinol* 21:1893–1904.

15. Bassett JH, et al. (2007) Thyroid hormone excess rather than thyrotropin deficiency induces osteoporosis in hyperthyroidism. *Mol Endocrinol* 21:1095–1107.

16. Bassett JH, et al. (2008) A lack of thyroid hormones rather than excess thyrotropin causes abnormal skeletal development in hypothyroidism. *Mol Endocrinol* 22:501–512.

17. Robson H, Siebler T, Stevens DA, Shalet SM, Williams GR (2000) Thyroid hormone acts directly on growth plate chondrocytes to promote hypertrophic differentiation and inhibit clonal expansion and cell proliferation. *Endocrinology* 141:3887–3897.

18. Barnard JC, et al. (2005) Thyroid hormones regulate fibroblast growth factor receptor signaling during chondrogenesis. *Endocrinology* 146:5568–5580.

19. Stevens DA, et al. (2003) Thyroid hormone activates fibroblast growth factor receptor-1 in bone. *Mol Endocrinol* 17:1751–1766.

20. Geoffroy V, Kneissel M, Fournier B, Boyde A, Matthias P (2002) High bone resorption in adult aging transgenic mice overexpressing cbfa1/runx2 in cells of the osteoblastic lineage. *Mol Cell Biol* 22:6222–6233.

21. Saftig P, et al. (1998) Impaired osteoclastic bone resorption leads to osteopetrosis in cathepsin-K-deficient mice. *Proc Natl Acad Sci USA* 95:13453–13458.

22. Doube M, Firth EC, Boyde A (2007) Variations in articular calcified cartilage by site and exercise in the 18-month-old equine distal metacarpal condyle. *Osteoarthritis Cartilage* 15:1283–1292.

23. Boyde A (2003) The real response of bone to exercise. *J Anat* 203:173–189.

24. Boyde A, et al. (1998) Effect of estrogen suppression on the mineralization density of iliac crest biopsies in young women as assessed by backscattered electron imaging. *Bone* 22:241–250.

25. Parfitt AM, et al., Report of the ASBMR Histomorphometry Nomenclature Committee (1987) Bone histomorphometry: Standardization of nomenclature, symbols, and units. *J Bone Miner Res* 2:595–610.

Fig. S1. Mechanical properties of D2KO and D1/D2KO bones at maximum load and fracture load. (*A*) Transverse section of 16-week femur at the middiaphysis (*Left*). Idealized approximation of the transverse section (*Right*) showing the anterior-posterior cortical thickness (Tap) and diameter (Dap) and the medial-lateral cortical thickness (Tml) and diameter (Dml) as determined by Faxitron analysis. The midcortical radius (r) was calculated as shown. (*B*) Area under the curve plots showing energy dissipated before maximum load (orange) and elastic stored-strain energy at maximum load (purple) in femurs from WT and D2KO mice undergoing three-point bend testing. Total work energy at maximum load equals the sum of the elastic stored and dissipated energies at maximum load. Quantitative analyses are shown in Fig. 1*C*. (*C*) Area under the curve plots showing the energy dissipated before fracture (orange) and the elastic stored-strain energy at fracture (purple) in femurs from WT and D2KO mice undergoing three-point bend testing. Total work energy at fracture equals the sum of the elastic stored and dissipated energies at fracture. The energy dissipated at fracture divided by the area of the fracture surface is the "toughness" of the bone. Quantitative analyses are shown in Fig. 1*C*.
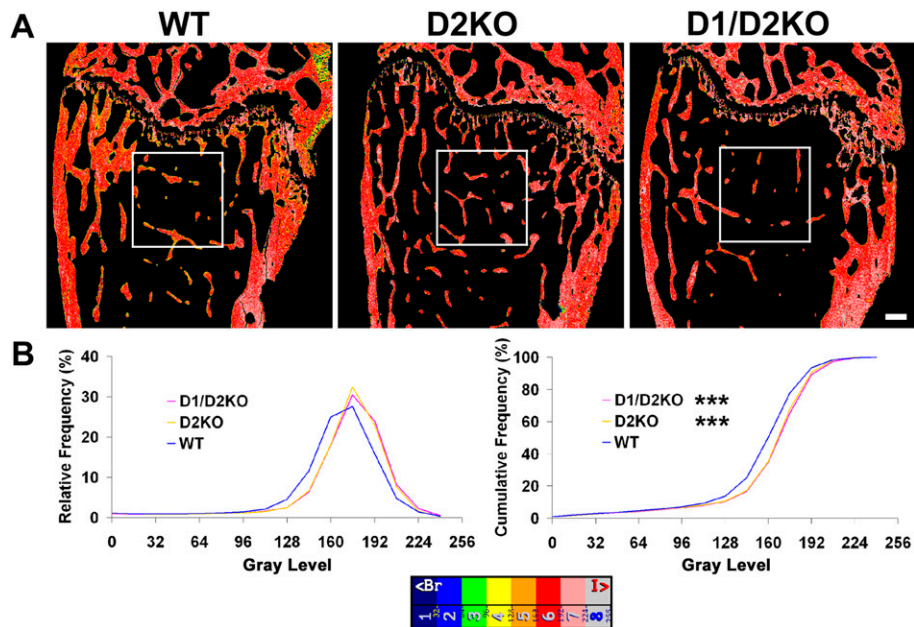
Fig. S2. Bone micromineralization density in long bones from D2KO and D1/D2KO mice. (*A*) Longitudinal sections of distal femur from PD112 WT, D2KO, and D1/D2KO mice imaged by qBSE-SEM (magnification ×33). Gray-scale images were pseudocolored according to an eight-color palette in which low mineralization density is blue and high density is gray. Boxes indicate trabecular bone regions of interest analyzed in the high-power views shown in Fig. 2*C*. (Scale bar, 200 μm.) (*B*) Relative and cumulative frequency histograms of combined trabecular and cortical bone micromineralization densities of femur, tibia, and humerus. Kolmogorov-Smirnov test; ***, $P < 0.001$ versus WT ($n = 4$).
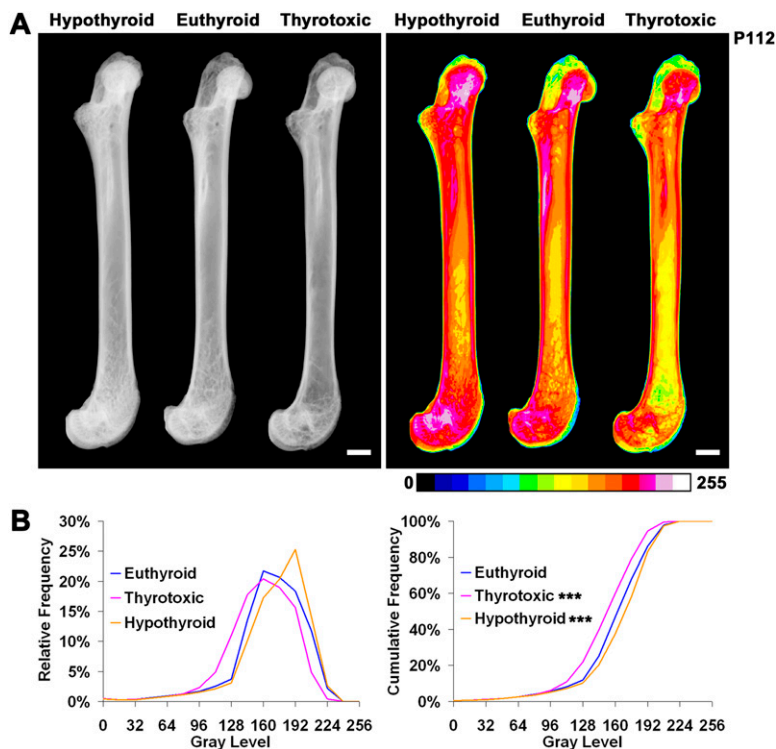
Fig. S3. Bone mineral content in adult male WT mice rendered euthyroid, thyrotoxic, or hypothyroid for 6 weeks before killing. Free thyroxine and free 3,5,3′-L-triiodothyronine levels were reduced by more than 60% in hypothyroid mice and were increased more than 10-fold in thyrotoxic animals. (*A*) Faxitron images of femurs from PD112 hypothyroid, euthyroid, and thyrotoxic mice. Gray-scale images were pseudocolored according to a 16-color palette; low mineralization density is black, high density is white. (Scale bar, 1000 μm.) (*B*) Relative and cumulative frequency histograms of mineralization densities from whole femur. Kolmogorov-Smirnov test; ***, $P < 0.001$ versus euthyroid ($n = 3$).

Fig. S4. In situ hybridization analysis of *Fgfr1* mRNA expression in (*A*) growth plate chondrocytes and (*B*) cortical osteoblasts from PD21 WT, D2KO, and D1/D2KO mice (representative data from studies of three mice per genotype).

Fig. S5. Bone development and midfemur cortical bone thickness of WT, D2KO, and D1/D2KO mice. (*A*) Upper limb paws from PD1 WT and D2KO mice stained with Alcian blue (cartilage) and alizarin red (bone). (*B*) Ribcages from PD1 WT and D2KO mice stained with Alcian blue and alizarin red. (*C*) Midfemur cortical bone sections from PD21 WT, WT+T3-treatment, D2KO, D2KO+T3-treatment, and D1/D2KO mice and from PD112 WT, D2KO, and D1/D2KO mice stained with Alcian blue and van Gieson (magnification ×50). (*D*) Quantitative analysis of cortical thickness in PD21 mice (*n* = 4).

Fig. S6. Measurement of serum markers of bone formation (*A* and *B*) and bone resorption (*C* and *D*) in PD91 male WT and D1/D2KO mice. Student's *t* test ($n = 7$). The age-related decreases in serum markers in male WT mice (mean $\pm$ SEM; $n = 5$) are shown in the right hand graphs. (*A*) N-terminal propeptide of type 1 procollagen (P1NP). (*B*) Osteocalcin. (*C*) C-terminal cross-linked telopeptide of type I collagen (CTX). (*D*) Tartrate-resistant acid phosphatase form 5b (TRAP).

Table S1. Biomechanical parameters of femurs from WT, D2KO, and D1/D2KO mice

Parameter	WT	D2KO	D1/D2KO
Yield load (N)	13.7 ± 1.1	16.5 ± 0.8	16.6 ± 1.4
Maximum load (N)	18.4 ± 0.8	19.9 ± 0.1	21.3 ± 1.7
Fracture load (N)	12.2 ± 1.2	**19.9 ± 0.1***	**19.7 ± 2.0****
Displacement at fracture (mm)	0.43 ± 0.03	**0.28 ± 0.02***	0.35 ± 0.03
Stiffness (Nmm)	74.7 ± 4.2	89.2 ± 6.7	90.7 ± 7.0
Young's modulus (GPa)	2.30 ± 0.19	3.00 ± 0.73	2.48 ± 0.21
Cross sectional moment of inertia (mm^4)	0.13 ± 0.02	0.12 ± 0.02	0.14 ± 0.02
Yield stress (MPa)	101.4 ± 9.3	126.8 ± 13.1	114.1 ± 9.7
Elastic stored strain energy at max load (Nmm)	2.26 ± 0.10	2.47 ± 0.24	2.51 ± 0.26
Elastic stored-strain energy at fracture (Nmm)	1.02 ± 0.18	**2.47 ± 0.24****	**2.17 ± 0.31***
Fraction of energy dissipated at maximum load (%)	30% ± 3%	20% ± 5%	34% ± 5%
Fraction of energy dissipated before fracture load (%)	79% ± 4%	**21% ± 5%*****	**46% ± 10%***
Toughness (N/mm^{-1})	4.47 ± 0.67	**0.61 ± 0.10****	**2.48 ± 0.46***
AP cortical thickness (mm)	0.21 ± 0.01	0.19 ± 0.01	0.22 ± 0.01
ML cortical thickness (mm)	0.25 ± 0.01	0.22 ± 0.01	0.23 ± 0.01
AP midshaft diameter (mm)	1.28 ± 0.06	1.24 ± 0.06	1.32 ± 0.05
ML midshaft diameter (mm)	1.67 ± 0.03	1.76 ± 0.04	1.72 ± 0.07

Force applied at mid point of a 5.6-mm span width. Statistical analysis: ± SEM; *, $P < 0.05$; **, $P < 0.01$ vs. WT; n = 3–6 per group; ANOVA with Tukey's multiple comparison post hoc test. AP, anteroposterior; ML, mediolateral.